On Collisionless Ion and Electron Populations in the Magnetic Nozzle Experiment (MNX)

S.A. Cohen,[a] X. Sun,[b] N.M. Ferraro,[a] E.E. Scime,[b] M.Miah,[a] S. Stange,[c] N. Siefert,[d] R.F. Boivin[e]

July 28, 2005

Abstract

The Magnetic Nozzle Experiment (MNX) is a linear magnetized helicon-heated plasma device, with applications to advanced spacecraft-propulsion methods and solar-corona physics. This paper reviews ion and electron energy distributions measured in MNX with laser-induced fluorescence (LIF) and probes, respectively. Ions, cold and highly collisional in the main MNX region, are accelerated along a uniform magnetic field to sonic then supersonic speeds as they exit the main region through either mechanical or magnetic apertures. A sharp decrease in density downstream of the aperture(s) helps effect a transition from collisional to collisionless plasma. The electrons in the downstream region have an average energy somewhat higher than that in the main region. From LIF ion-velocity measurements, we find upstream of the aperture a presheath of strength $\Delta\phi_{ps} = {}_{mr}T_e$, where ${}_{mr}T_e$ is the electron temperature in the main region, and length ~ 3 cm, comparable to the ion-ion and ion-neutral mean-free-paths; immediately downstream of the aperture is an electrostatic double layer of strength $\Delta\phi_{DL} = 3 - 10\ {}_{mr}T_e$ and length $0.3 - 0.6$ cm, $30 - 600\lambda_D$. The existence of a small, *ca.* 0.1%, superthermal electron population with average energy $\sim 10\ {}_{mr}T_e$ is inferred from considerations of spectroscopic line ratios, floating potentials, and Langmuir probe data. The superthermal electrons are suggested to be the source for the large $\Delta\phi_{DL}$.

I. Introduction

Helicon plasmas have been extensively studied in laboratories for over thirty years[1, 2] to elucidate the physics of wave propagation and plasma generation and to develop techniques for the plasma processing of materials, especially for the fabrication of semiconductor devices[3, 4] and for the destruction of toxic waste[5]. These applications are possible because the plasmas generated by the absorption of helicon waves are steady state, may reach densities of $n_e = 10^{14}$ cm^{-3}, and are of relatively low temperature, $T_e = 1 - 10$ eV, parameters that result in relatively high rates for surface modification and gas-phase ionization and decomposition at modest power consumption.

The good efficiency of helicon sources in producing dense plasmas[6, 7] has brought attention to a new application, improving spacecraft-propulsion methods, particularly for missions to remote planets[8, 9]. For this application, high propellent (plasma) flow speeds and high directionality are desired for the rocket exhaust stream, to enable the spacecraft to reach high speeds[10, 11]. Collisionless plasmas are expected in the exhaust stream of advanced propulsion systems, in large part due to expansion of the plasma jet. For magnetized plasmas used for propulsion, collisionless processes must enable the plasma jet to detach from the rocket engine's magnetic field[12]. This

is a subject of on-going research[13, 14]. As shown in this paper, the transition from collisional to collisionless occurs in the denser region, near the plasma source.

A figure-of-merit for propulsion is the specific impulse, $I_{sp} \equiv v/g$, where v is the directed flow velocity of the plasma and g is the acceleration of gravity, 9.8 m/s^2. Chemical rockets achieve I_{sp} as high as 500 s; propulsion methods which employ plasma or ion beams have achieved $I_{sp} > 10^4$ s[10]. (An I_{sp} of 3000 s, corresponding to an energy of $\sim$ 4.5 eV/amu, is considered the minimum requirement for many remote-planet missions.)

Other yardsticks for advanced spacecraft-propulsion technologies include energy and fuel-utilization efficiencies and thrust. Too high an I_{sp} gives less thrust *per* unit of power, hence limits on and control of I_{sp} are required, with values set by the specific demands of each spacecraft mission and the capability of each spacecraft. In many advanced propulsion systems, energy efficiency will depend on the transport characteristics of collisionless plasmas. Another important factor determining energy efficiency is the energy "wasted" in ionization. To lower the ionization-energy penalty, it is advantageous to accelerate massive singly ionized atoms to higher energy than to accelerate light multiply charged ions to lower energy. The results described herein concentrate on argon plasmas – with occasional helium doping for spectroscopic diagnostic purposes – though xenon would offer an advantage in energy efficiency.

The question arises of how to accelerate argon ions to 180 eV, *i.e.*, an I_{sp} of 3000 s. One promising approach is the use of ion cyclotron-resonance heating[15, 16]. Our experiments follow a different path made evident by the discovery of a natural phenomenon in high-density helicon plasmas, the formation of strong electrostatic double layers which accelerate ions into directed beams having supersonic speeds[13, 17]. Double layers have been observed in earlier low-density experiments[18, 19, 20, 21, 22, 23, 24] and recently[25, 26] in other helicon devices. This alternate path allows a small scale, low cost, relatively simple experimental facility to explore many physics issues of flowing collisionless plasmas.

In Section II we describe the experimental facility and the laser-induced-fluorescence (LIF), spectroscopic, and probe diagnostics. Section III, IV, and V present ion and electron distributions and spectroscopic line ratios measured in MNX, respectively. Section VI discusses the results and presents plans for future research.

II. Experimental setup

The experiments were performed in the Magnetic-Nozzle-Experiment device (MNX), see Fig. 1a). Steady-state argon plasma is formed by the helicon technique. The antenna, a double-saddle design, is placed around a 4-cm-ID, 30-cm-long Pyrex tube; RF power, at 26.75 MHz, is provided to a T-type tank circuit with the antenna as inductor. The 4−cm-diameter plasma thus formed flows along the magnetic field formed by a Helmholtz-coil pair placed coaxially around the 45-cm-long, 20-cm-ID, stainless-steel main chamber. An iron plug placed on the endplate of the 30-cm Pyrex tube helps shape the magnetic field inside the tube. (Several endplate designs have been used. The present one is a reentrant carbon-fiber-composite cup which reducing sputter-coating of the Pyrex tube with endplate material.) Each Helmholtz coil consists of 11 pancake coils which may be wired in any combination, allowing axial fields as high as 4 kG in the center of the main chamber, corresponding to 5.5 kG in the midplane of a Helmholtz coil. Plasma and device parameters of MNX are summarized in Table I.

The plasma exits the main chamber through the coaxial 2-cm-ID, 3-cm-long nozzle coil used

to control the field gradient and mirror ratio. The maximum steady-state on-axis magnetic field the nozzle coil produces is 2.5 kG. Fig. 1b) shows possible lines-of-sight for LIF collection optics used to view the plasma exiting the nozzle coil. Fig. 1c) shows the axial field strength near the nozzle at a Helmholtz coil current of 50 A and nozzle current of 400 A, typical of experimental conditions in this paper. The current capability of both the Helmholtz and nozzle coils is 440 A.

Exiting the nozzle coil, the plasma enters a 10-cm-ID, 100-cm-long Pyrex tube termed the expansion region (ER). The ER has 15 internal 4-cm-ID, 0.3-cm-thick coaxial copper rings, of which 8 may be electrically biased. Additionally there are 3 metal discs, labeled *endplate*, $M2$, and $M3$ in Fig. 1a, which may be electrically biased. (In the experiments described here, unless specificially noted otherwise, the endplate, M2, and M3 were left electrically floating. Biasing the endplate or M3 had little effect on the LIF results; connecting the endplate or M2 to ground required more RF power input to sustain the plasma.) M2 has an 0.24 to 1.0-cm-ID aperture hole which limits both the plasma and neutral gas flow into the ER. The axial location of M2 and the size of its aperture have been varied, to explore the roles of field gradients and mechanical apertures on double-layer (DL) parameters. In the absence of plasma and in conjunction with the ER pump, (P2, see Fig. 1a), the low conductance of M2 maintains up to a $\times 10$ lower pressure in the ER compared with the main chamber. Closing valves V1, V2 and/or V3, or leaking gas into the ER, allows controlled increase of the pressure in the ER. Pressures are measured in the main chamber and the ER by capacitance manometers with accuracies of ± 0.1 and ± 0.001 mT, respectively. These pressure gauges allow measurement of plasma flow into the ER.

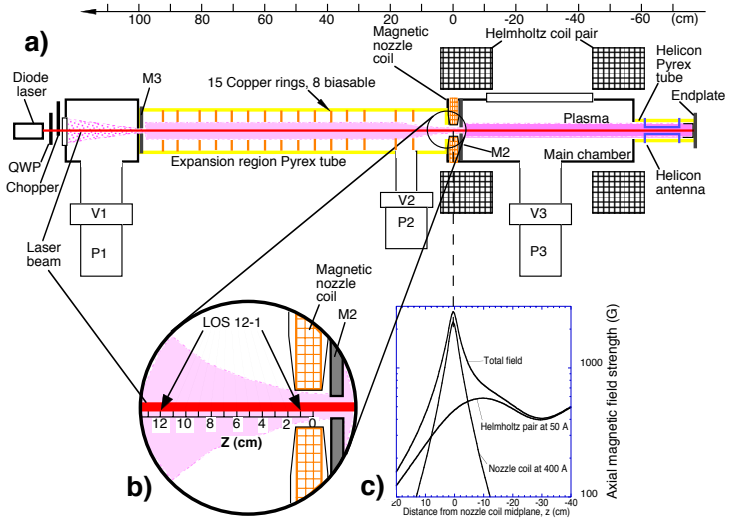

Figure 1: Schematic of MNX. a) Argon plasma is formed by absorption of helicon waves launched from a double-saddle antenna. The plasma flows through the main chamber along magnetic field fines created by a set of Helmholtz coils. The plasma then flows through the aperture in M2 and the nozzle coil into the expansion region (ER). The beam of a diode laser is directed along the MNX axis, allowing LIF measurements throughout MNX. Scanning Langmuir probes are located in the center of main chamber and at three positions, $z = 12,\ 24$ and 70 cm, in the expansion region. b) A scanning mechanism for the LIF collection optics allows 12 lines-of-sight (LOS) intercepting axial points in the ER near the nozzle. Other LOS are in the main chamber. c) On-axis axial magnetic field strength near the nozzle coil.

At low Helmholtz fields, $B_H = 200 - 1200$ G, MNX operates stably in the "blue-core" helicon mode over a wide range of main-chamber pressures, from 0.4 to above 30 mT, at RF powers from 200 to over 2000 W. The blue core, about 2 cm in diameter at $B_H = 400$ G, decreases in size as the field is increased, reaching 0.3 cm at $B_H = 2.5$ kG and then increases in size. Most results

described herein were obtained near the lowest main-chamber neutral pressure, to reduce collisional de-excitation of the Ar^{*+}, the species necessary for the LIF signal.

The Langmuir probe in the main chamber is a single probe of cylindrical shape with radius 0.025 cm. A 1.9-MHz low-pass filter is used to eliminate RF pickup. Radial scanning is accomplished by a pneumatic drive. Langmuir characteristics, over a voltage range from -140 to +60 volts, are acquired at 10-100 Hz, providing a spatial resolution as small as 1 mm. Langmuir probe spatial scans in the main chamber, described in more detail in Section III, show that the plasmas achieved peak ion densities up to 5×10^{13} cm^{-3} and electron temperatures in the range 2 to 10 eV. The line-averaged electron density is measured by a 170-GHz interferometer directed across a major chord in the center of the main chamber. The interferometer confirmed the probe-measured density to within 20%. Langmuir probes in the ER are paddle-shaped single probes, coated with boron nitride on one side. Negligible RF is detected in the ER.

Table 1: Plasma and device parameters of MNX.

Parameters	main region	expansion region
B (kG)	0.5-5.5	8-0.02
L (cm)	70	100
n_e (10^{13} cm^{-3})	0.1-5	0.1-10^{-4}
p_n (mT)	0.4-20	0.1-20
RF heating power (W)	50-2000	
ω_{pe} (10^{10} rad/s)	5.6-40	5.6-0.18
ω_{ce} (10^{9} rad/s)	9-100	145-0.35
ω_{ci} (10^{6} rad/s)	0.12-1.3	2-0.005
Probe radius, r_p, (cm)	0.025	0.5
Plasma radius, R, (cm)	2	0.1-4
Debye length, λ_D, (cm)	$2 \times 10^{-3} - 1.5 \times 10^{-4}$	$7 \times 10^{-2} - 1.8 \times 10^{-3}$
Ion gyroradius, ρ_i, (cm)	1-0.025	0.015-45
Electron gyroradius, ρ_e, (cm)	$1.3 \times 10^{-2} - 6 \times 10^{-4}$	$0.4 - 7 \times 10^{-4}$
T_e (eV)	2-10	6-20
$E_{e,max}$ (eV)		220
$E_{i,\|\|}$ (eV)	0.04-0.6 (8 in presheath)	0.06-80.
$T_{i,\|\|}$ (eV)	0.03-0.4	0.04-2.
$E_{i,\perp}$ (eV)	0.04-0.9	
$T_{i,\perp}$ (eV)	0.03-0.6	
λ_{ii} (cm)	$2 \times 10^{-5} - 0.1$	$2 \times 10^{-2} - 7 \times 10^{3}$
λ_{ee} (cm)	0.09-100	35-10^5
λ_{en} (cm)	0.3-15	0.3-60
λ_{in} (cm)	0.1-5	0.1-20

To permit measurement of the field-parallel Ar^{+*} velocity distribution in MNX, the elliptical-cross-section (5 mm×1 mm) tuneable diode-laser beam is directed along the MNX magnetic axis. (To measure the perpendicular velocity in the main chamber, the laser beam was directed perpen-

dicular to the magnetic field in the main chamber, not shown in Fig. 1.) Optics to collect the fluorescence emission are located on both the main chamber and the expansion chamber. Main-chamber LOSs collect photons from a selectable 5 mm^3 volume near the center of the chamber downstream to M2. Scanning optics on the ER allow LOSs which intercept the laser beam from 1-cm from the nozzle-coil midplane to 12 cm from its midplane, as well as beyond, see Fig. 1b). LIF measurements in nozzle field gradients are relevant to the physics of the solar corona[27].

The laser used for LIF is a 1.5-MHz-bandwidth Sacher LaserTechnik diode laser, which may be coarse tuned in wavelength from 662 to 674 nm, allowing excitation of the 668.614 nm (zero-field, vacuum) transition $3d^4F_{7/2} - 4p^4D_{5/2}$ of Ar^{+*}[28, 29]. Finer tuning, over a maximum 0.4 nm wavelength range, is accomplished, manually or automatically, by changing the voltage on the laser's internal piezoelectric crystal. A photomultiplier with 1-nm transmission filter centered at 442.7 nm (vacuum) collects emission from the 442.7 nm fluorescence transition, $4p^4D_{5/2} - 4s^4P_{3/2}$, with Einstein coefficient $A = 9.856 \times 10^7 s^{-1}$[30]. The Zeeman effect from the Helmholtz and nozzle-coil fields separates the 668.614 nm transition into six $+\sigma$, six $-\sigma$, and six π sub-components. Because of Doppler broadening, the 6 sub-components of each merge into single peaks called the $+\sigma$, $-\sigma$, and π components. (An axially propagating laser only excites the σ components.) To reduce the complexity of the LIF spectrum and increase signal/noise (S/N), the linearly polarized laser beam may be passed through a quarter-wave plate (QWP), oriented to convert the beam into either right- or left-circularly polarized (RCP, LCP) light for exciting either the + or $-\sigma$ transitions. (For measurements of the perpendicular velocity, the laser beam is linearly polarized, parallel to the magnetic field.) The laser beam is modulated at $\sim$ 4 kHz by a mechanical chopper, for lock-in detection of the 442.7 nm fluorescence. This LIF system operates well within the unsaturated mode wherein the LIF signal is proportional to the laser intensity and the $3d^4F_{7/2}$ metastable population in the detection volume that is in resonance with the laser. A single wavelength scan is usually limited to a mode-hop-free region of 0.021 nm (14 GHz) and is performed in $\sim$ 60 seconds; 1000 data points are recorded. Simultaneous with each wavelength scan, laser power and wavelength are recorded using a ThorLabs powermeter and a Burleigh 1500 wavemeter (resolution = $\pm$0.0001 nm), respectively. A set of observations of a single plasma condition typically includes scans over several adjacent wavelength regions in the range 668.580 to 668.660 nm, both with and without the QWP inserted. Using orthogonal QWP orientations allows the Zeeman splitting to be measured and the unshifted line center to be identified.

The primary diagnostic for emission spectroscopy is a 1/2 m J-A spectrometer, equipped with a 256 $\times$ 1024-pixel Princeton Instruments iCCD. Three gratings are mounted in the spectrometer: 600, 1200 and 2400 l/mm. The spectrometer is fiber-optic coupled to view the plasma using the same collection optics as the LIF system. Electron temperatures are extracted from the data using neutral-helium line ratios interpreted with a collisional-radiative model[31]. Accordingly, for these measurements helium is added to the argon plasmas.

III. LIF-measured ion populations

The Ar^{*+} perpendicular temperature was measured on-axis in the center of the MNX main chamber using LIF on the π component. Fig. 2a) shows one LIF spectrum. A deconvolution technique[32] was used to extract the temperature and ion flow velocity. The ions are relatively cool and have negligible radial flow velocity. The red curve shows the best fit of a Gaussian to the data, giving $T_{i,\perp} = 0.24$ eV. Ion temperature was measured at a variety of RF power levels and Ar fill pressures. Fig. 2b) shows the ion temperature *vs.* RF power at a fill pressure of 5 mT. At low power the plasma is in the inductively coupled (so-called "purple") mode. The threshold

for the transition to blue-core depends on the fill pressure, with lower powers being required at higher pressures. Fig. 2c) shows that ion temperature increases with decreasing p_n. At the lowest operating pressure where a stable helicon discharge could be sustained with this antenna system, 0.4 mT, the ion temperature reached 0.6 eV. As noted later, the plasma density in MNX's "blue-core" mode is about 10^{13} cm^{-3}; these ions are highly collisional, with a Coulomb mean-free-path, λ_{ii}, less than 1 mm.

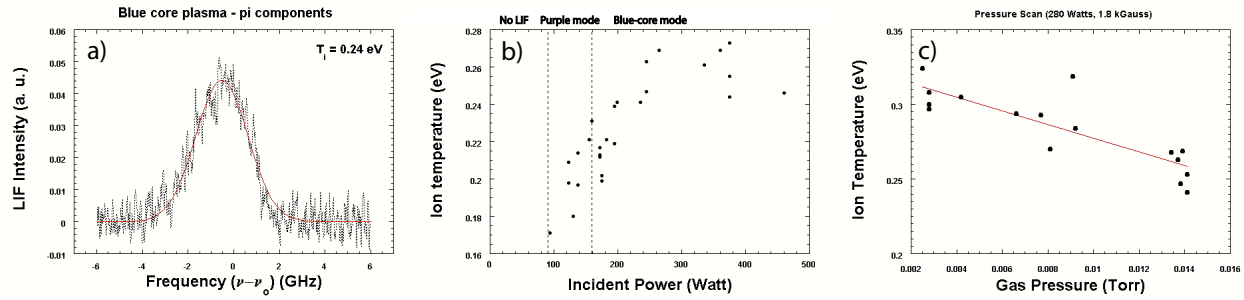

Figure 2: a) LIF intensity *versus* laser frequency, ν, in the center of the MNX main chamber. ν_o is the frequency of the non-Doppler-shifted line. The uncertainty in the value of ν_o is 0.5 GHz. b) $T_{i,\perp}$ *versus* RF power. At this argon fill pressure, the plasma makes a transition from inductive (purple) to helicon (blue-core) mode at powers above 160 W. Though plasma exists at powers as low as 20 W, the LIF signal is too weak to provide a good measurement of ion temperature. c) $T_{i,\perp}$ *versus* argon fill pressure.

The parallel ion energy distributions *versus* axial position near the center of the MNX main chamber were measured along the axis of MNX, Fig. 3a), using the σ components[33]. To allow better lines-of-sight for the LIF optics, M2 was re-located to near the center of MNX by placing it on a long metal cylinder attached to the nozzle coil, see Fig. 3a) inset. The data shown were obtained using collection optics 3. At a position 7 cm from M2, the ions are cold, $T_{i,\|} \sim 0.2$ eV, and unflowing. The ion flow velocity (energy) rises closer to M2, reaching 5 eV, $\sim T_e$, at 1 mm from M2. This region of ion acceleration is the presheath; its length, ~ 3 cm, is close to the ion-neutral charge-exchange mean-free-path, λ_{in}, and to λ_{ii}. The ion temperature, both parallel and perpendicular, is of order 0.1-1 eV, allowing the pre-sheath ions to equilibrate with each other.

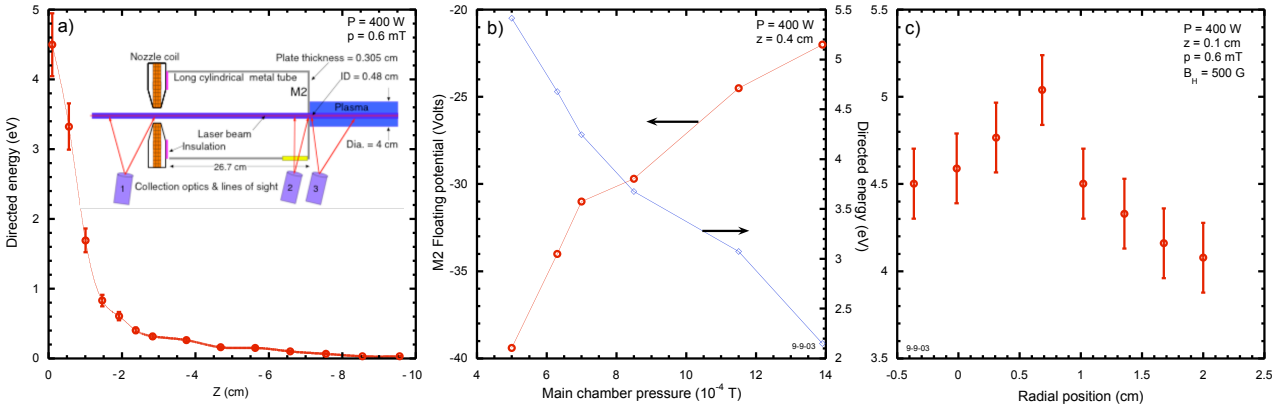

Figure 3: Z-directed argon-ion energy, E_z, in the MNX main chamber for $P_{RF} = 400$ W. a) E_z near M2 *versus* z, using collection optics 3, as shown in the inset. Note that M2 was relocated to near the center of MNX's main chamber and the diameter of the aperture was set to 0.48 cm. b) Variation of E_z (at z = 0.1 cm) *versus* main chamber pressure. The floating potential of M2 becomes more negative with decreasing pressure. c) Variation of E_z *versus* radial position. The LIF collection optics viewed at the aperture and the plasma column was shifted upwards by addition of a vertical magnetic field.

The maximum z-directed energy, E_z, attained by ions in the presheath decreases with increasing pressure, see Fig. 3b). As shown in Section IV, the electron temperature in this low pressure range drops with increasing neutral pressure; the ion energy at the aperture remains $\sim T_e$. Also shown in Fig. 3b) is the floating potential of M2, ${}_{M2}V_f$. At a power of 1 kW ${}_{M2}V_f$ has fallen to about -50 Volts at $p_n = 0.6$ mT.

The plasma column may be shifted vertically or horizontally by addition of fields provided by pairs of coils positioned outside the Helmholtz coils. Using this capability, the plasma column was moved vertically while E_z was measured 1 mm from the aperture. The presheath E_z radial profile is slightly hollow, see Fig. 3 c). ${}_{M2}V_f$ remained constant at -32.1 Volts.

We have explored the effect of M2 location on the energy of the downstream Ar ions by placing M2 at 4 locations, three at various distances (0.1, 1.9 and 26.7 cm) upstream of the magnetic nozzle and one 3 cm downstream of the nozzle[33]. We have also removed M2 completely, allowing the nozzle coil, either through its magnetic field or its 2-cm inner diameter to act as an aperture for the 4-cm-dia Ar plasmas. The results for these five cases are qualitatively the same, though important differences occur. Herein we review the primary common feature, the acceleration of ions to supersonic speed. In conjunction with a sharp decrease in density downstream of M2, these higher energy ions are collisionless.

Fig. 4a) shows the LIF spectral distributions for both RCP and LCP laser beams. Two + σ and two - σ peaks are seen. The +/- pair with little frequency shift are termed the low energy peaks (LEP); the Doppler shift of their average frequency shift is subthermal. The +/- pair with large frequency shift are termed the high energy peaks (HEP). The parallel temperatures of the LEP and HEP ions are about 0.1 eV and 1 eV, respectively. E_z of the HEP increases with distance downstream of the nozzle coil, see Fig. 4b). Energies over 70 eV have been observed, depending on the placement of M2, the RF power, and the gas pressure in both the main chamber and the ER. (Efforts to reach the 180 ev target, *i.e.*, an I_{sp} of 3000 s, are being made.) Increasing gas pressure in the ER decreases the amplitude of the HEP signal while raising that of the LEP, see Fig 4c). With M2 placed in different locations for better LIF access, the length of the region of acceleration to an energy above $2T_e$ has been measured to be $0.3 - 0.6$ cm.

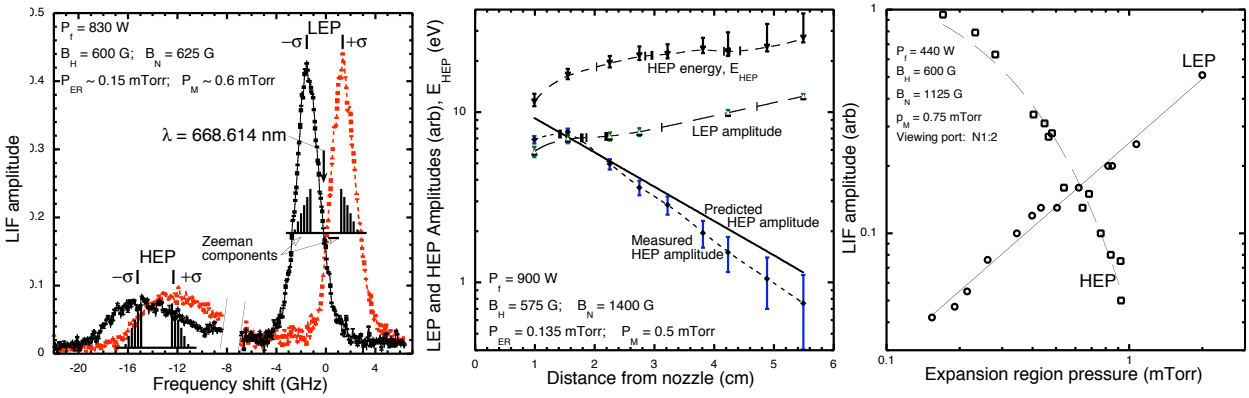

Figure 4: a) LIF amplitude *versus* frequency shift in the ER, 2 cm downstream from the nozzle midplane. The frequency zero is the non-Doppler-shifted line. The red (black) data are for RCP (LCP) laser beam. The 6 Zeeman + and - σ subcomponents merge into single peaks. Two sets of peaks are labeled, HEP and LEP. b) HEP amplitude and E_z and LEP amplitude *versus* distance downstream from the nozzle coil. c) HEP and LEP amplitudes *versus* argon pressure in the ER at 2 cm from the nozzle-coil midplane.

As discussed in Ref[13], the cause of the LEP is plasma created in the ER by electron impact ionization. In contrast, the HEP ions were created in the main chamber (as cold ions) and accelerated through a double layer formed just down stream of M2 or the nozzle coil. The decrease in HEP amplitude in the ER, see Fig. 4b) is slightly faster than predicted by a model which includes magnetic -field divergence, ion acceleration (*i.e.*, the continuity equation), and de-excitation of the Ar^{*+}'s by collisions with neutrals. The mean-free-path of the HEP ions against charge exchange is as long as 30 cm and against Coulomb collisions is greater than several meters while the LEP ions remain collisional until the density falls below 10^{10} cm^{-3}. The ER plasma thus consists of both collisionless and collisional ions populations, the former flowing through the latter at supersonic speed.

One goal of the MNX program is to explore the analogy between a magnetic nozzle and a Laval nozzle. Fluid – even multicomponent – upstream of a Laval nozzle is generally in thermal equilibrium. The perpendicular component of the fluid's thermal energy gets converted by the nozzle to directed energy. In the MNX main chamber, collisional coupling is weak between electrons and ions and there is no thermal equilibration between them; the ions are much cooler than the electrons. The gain in energy by the ions as they transverse the nozzle is far more than the conversion of their own perpendicular energy to parallel energy. They are gaining energy from the electrons, with a sizable fraction of the energy gained in a region short, *ca.* $100\lambda_D$, compared to the nozzle field curvature. From measurements described in Section IV, we shall see that the energy gained by an ion is greater than that available from a thermal electron. To elucidate the energy-gain process, we present here effects of nozzle field strength on the ion energy.

Fig. 5 shows the E_z for ions downstream of M2 *versus* nozzle field strength, B_n, for three locations of M2. For M2 placed immediately upstream of the nozzle coil, see Fig. 5a) inset, the directed ion energy of the HEP ions first falls 10% with increasing B_n to 500 G then slowly rises 5% as B_n reaches its maximum value. Fig. 5b), with M2 placed 3.1 cm downstream of the nozzle coil shows much more dramatic reduction in the E_z of the HEP ions – by more than 50% whether 1 mm from the M2 aperture, z = 3.2 cm, or 0.8 cm further downstream, at z = 4.0 cm. Fig. 5b) also shows that the brightness of the HEP increases with B_n, an indicator that more ion flux is channelled through the nozzle coil with increase in B_n, *i.e.*, $B/n_e \sim$ constant.

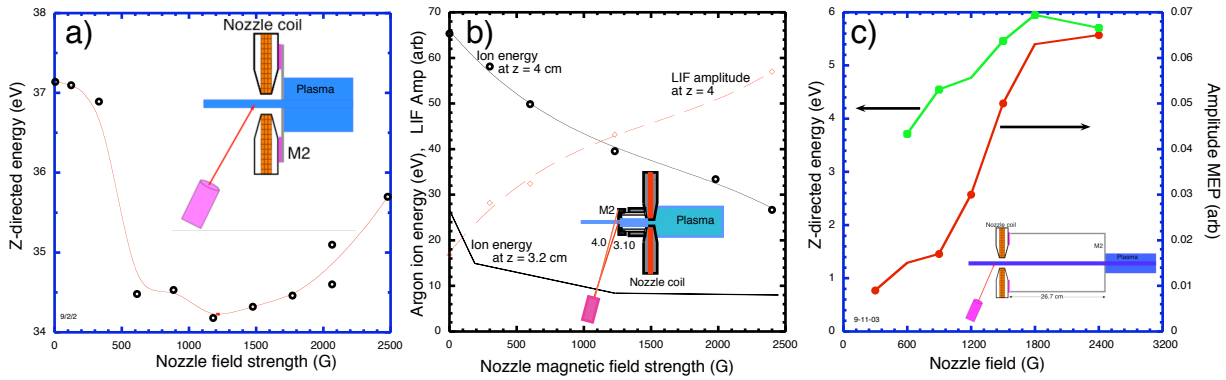

Figure 5: a) E_z of the HEP ions *versus* nozzle field strength at z = 2 cm in the ER. The plate M2 was located 1 cm upstream of the nozzle coil midplane, as shown in the inset. b) HEP E_z *versus* nozzle field strength at z = 3.2 and 4.0 cm from the nozzle-coil midplane. M2 was located 3.1 cm downstream of the nozzle-coil midplane, see inset. c) E_z of the MEP ions *versus* nozzle field strength at z = 2 cm from the nozzle-coil midplane. M2 was located 26.7 cm upstream of the nozzle-coil midplane, see inset.

The data in Fig. 5c) require a bit more explanation. With M2 placed well upstream of the nozzle coil, at z = -26.7 cm, three sets of peaks are observed in the LIF spectrum in the ER. The HEP and LEP have already been discussed. Appearing at an intermediate energy is a third set of peaks called the MEP, medium energy peaks[33]. These are ascribed to plasma formed within the long metal cylinder. The energy of these MEP ions grows 50% as B_n increases to 2.5 kG. The MEP amplitude grows faster than B_n, one indicator that these ions are formed by ionization, *i.e.*, $\propto n_e^2$.

Changing B_n has little effect on the ion temperature and flow in the main chamber. In the next section we show that B_n also has little effect on the temperature and density of the "bulk" electrons in these plasmas.

IV. Electric-probe-measured electron populations

The probe data to be presented show that the ratio of the probe radius, r_p, to the Debye length, λ_D, is large, *ca.* 100, in both the main chamber and the ER. That fact, combined with the LIF observations that no plasma drift occurs in the main chamber (except in the presheath), allows the Laframboise equations for cylindrical probes to be used in the main chamber to evaluate the Langmuir probe data. An important feature of the Laframboise equations for large r_p/λ_D is a flat ion-saturation current with increasingly negative bias. The main-chamber Langmuir-probe characteristics often show a small tail extending to high energy, above 100 eV. We do not discuss that data here, due to the lack of certainty that RF is not affecting the characteristics. Instead we describe the bulk electron parameters in the main chamber and then the tail in the ER probe characteristic where RF effects are clearly unimportant.

The bulk electron populations may be characterized by temperature, density, and ion saturation current. How these depend on magnetic field, main-chamber neutral pressure (p_n), and RF power (P_{RF}) are shown in Fig. 6. All data are from blue-core-mode helicon discharges. Fig. 6 consists of 8 graphs in two columns. Graphs in the left column are of ion saturation current *versus* radius, with the probe biased at -60 V. Ion saturation current, I_{sat}, is plotted instead of density because it is acquired with better spatial resolution. Also, the electron temperature is nearly constant across the radius, so I_{sat} gives a good relative measure of $n_e(r)$. The graphs in the right column are of the central values of plasma density and electron temperature *versus* the independent variables: main chamber pressure, a) and b); RF-power coupled, c) and d); nozzle-coil current, e) and f); or Helmholtz- (main)-coil current, g) and h). In all cases, the I_{sat} radial profiles are peaked. Considerable plasma exists beyond $r = 2$ cm, the nominal plasma edge defined by the ID of the Pyrex section inside the helicon antenna.

The data for Fig. 6a) and b) were acquired at a $P_{RF} = 800$ W, $B_n = 0$ G, and $B_H = 500$ G. The electron temperature is highest at low p_n. This is consistent with the model of plasma formation based on a balance between sheath-limited particle and energy losses and volumetric ionization[3]. The density is low at low and high p_n. The data for Fig. 6c) and d) were acquired at a $p_n = 2.5$ and 0.7 mT, $B_n = 0$ G, and $B_H = 500$ G. The electron temperature is nearly independent of P_{RF} while the density rises monotonically with P_{RF}, again consistent with Ref. [3]. The data for Fig. 6e) and f) were acquired at a $P_{RF} = 800$ W, $p_n = 0.7$ mT, and $B_H = 500$ G. The electron temperature falls slightly with B_n while the density rises. Energy confinement remains constant. The data for Fig. 6g) and h) were acquired at a $P_{RF} = 800$ W, $p_n = 0.7$ mT, and $B_n = 0$ G. The electron temperature depends little on Helmholtz-coil current, I_H. The density falls precipitously for $I_H < 80$ A. We are unable to sustain helicon discharges at $I_H < 37$ A.

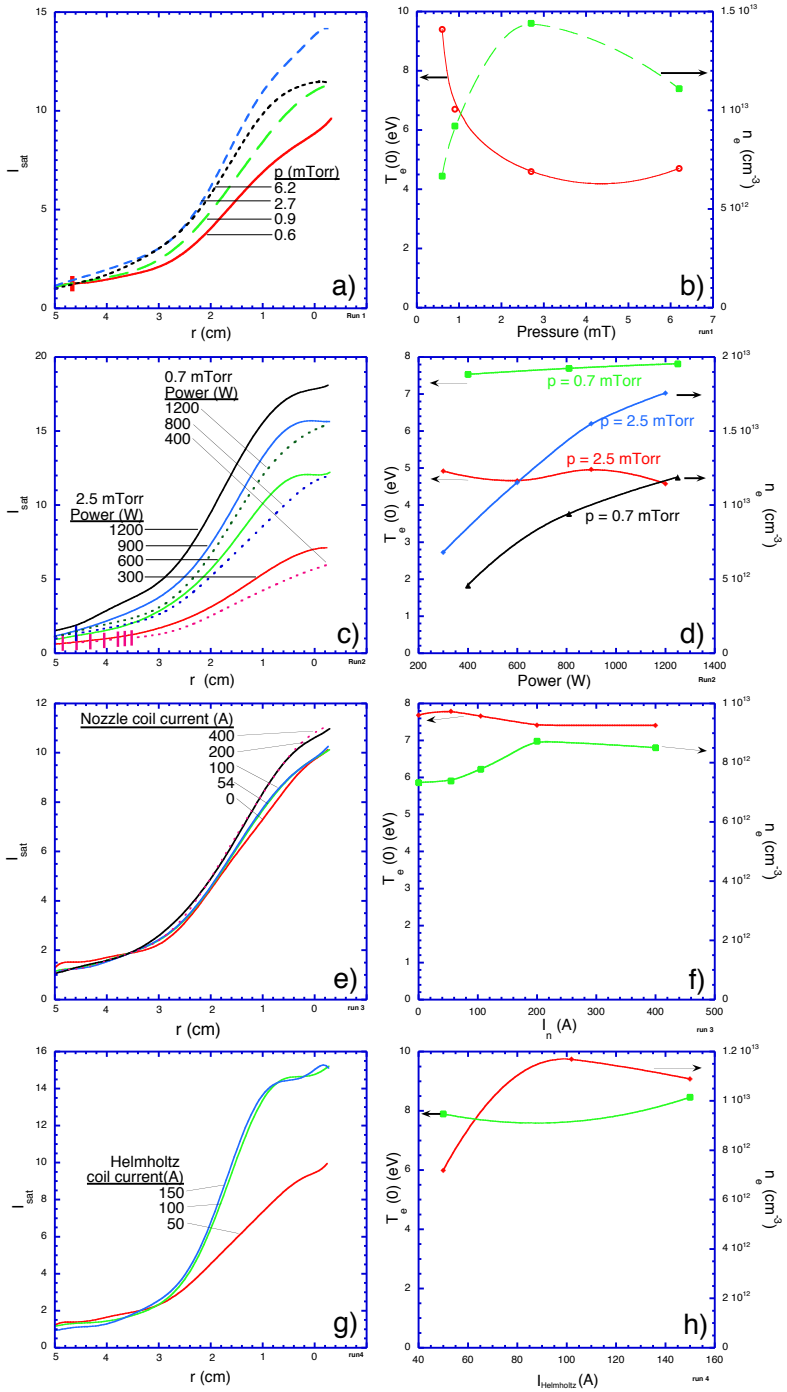

Figure 6: Radial dependance of ion saturation current and dependences of central electron temperature and density of bulk plasma in center of MNX main chamber *versus* main chamber pressure, RF power, nozzle-coil current, and Helmholtz-coil current.

Langmuir-probe characteristics obtained with a paddle probe located in the ER at z = 12 cm from the nozzle coil are shown in Fig. 7 for Ar plasmas. A constant ion-saturation current was subtracted from the probe current. The operating parameters were nearly the same for both a) and b), with the exception that the nozzle coil was used while taking the data in Fig. 7b). Without the nozzle coil powered, a clear two-temperature Maxwellian is seen; with the nozzle coil powered, the

separation in temperatures in less pronounced and the bulk electrons are warmer. Recall that E_z in the ER dropped with increasing B_n. The tail temperature is strongly dependent on the exact value of the saturation current subtracted. If a higher ion-saturation current is subtracted, the tail loses its Maxwellian shape - exponential decrease with V_{bias} - and a higher average energy is inferred.

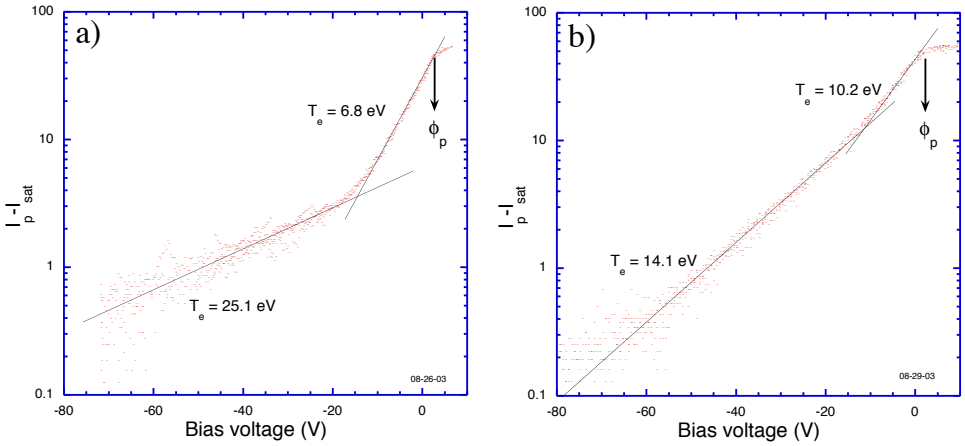

Figure 7: Langmuir probe characteristics in the ER. $P_{RF} \sim 900$ W, $p_n \sim 0.7$ mT, $B_H \sim 700$ G. a) No nozzle field. b) With 2 kG nozzle field. Error bars: $\pm 3\%$ for bulk T_e; $\pm 20\%$ for tail T_e

We now describe electrical measurements on macroscopic structures in MNX and how they indicate the presence of fast electrons in the main chamber. Fig. 8a) adds M2 (aperture-plate) floating potential, ${}_{M2}V_f$, and the ER pressure, p_{ER}, results to data previously presented on the HEP ion energy, E_z, in the ER with the M2 aperture plate positioned at 3.1 cm in the ER, see inset Fig 5b). The pressure in the ER increases with B_n, indicating increasing plasma flow through the M2 aperture. $|{}_{M2}V_f|$ and E_z both decrease with increasing B_n. Note that ${}_{M2}V_f \sim 10T_e$ in the main chamber, about twice the value expected based on the data in Fig. 6. This is a signature of a superthermal electron component in the main chamber[34, 22, 24, 35]. In simple terms, when the fast electron flux is comparable to the ion flux, the bulk electrons are not needed to balance the ambipolar flow to objects immersed in the plasma; the objects will charge to a higher floating potential, approaching the energy of the fast electrons. For argon plasmas this would occur at a fast electron density above $\sqrt{m_e/M_i}\ n_e \sim 0.003\ n_e$[35, 34].

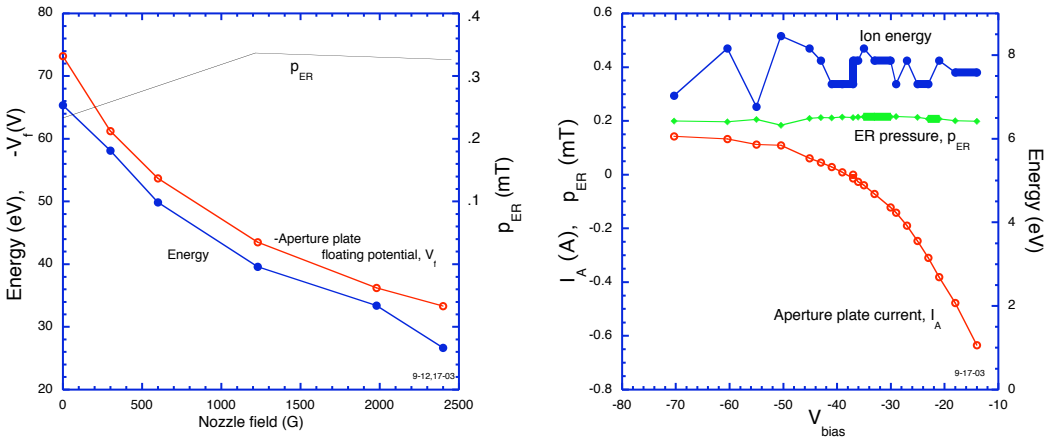

Figure 8: a) Dependence on nozzle field strength of ER pressure, M2 floating potential and HEP E_z at z = 4 cm in the ER. b) ER pressure, HEP E_z (at z = 3.2 cm) and M2 (aperture-plate) current *versus* bias voltage applied to M2. For geometry, see inset Fig. 5b).

An immediate question is whether the M2 potential sets the ion energy or is result of the same phenomenon that generates high energy ions. Fig. 8b) shows that the M2 potential is not the cause of ion acceleration. The ion energy measured at $z = 3.2$ cm barely changes as the voltage applied to M2 – using the main-chamber stainless-steel vessel as ground – is varied both above and below the floating potential, -40 V. The constancy of p_{ER} shows that the aperture plate voltage barely affects the plasma flow into the ER. Fig. 8b) also shows that the presheath potential, as determined from E_z in the aperture, *ca.* 8 eV, is hardly affected by biasing M2.

In the ER are placed 15 copper rings – also called flux conservers – coaxial with the MNX major axis and separated from each other by 1.1-1.3 cm. Eight of the rings are electrically biasable and instrumented to measure currents or floating potentials, see Fig. 9a). Floating potentials, ${}_rV_f$, of the rings were measured with M2 placed either in the ER or in the MC. Fig. 9b) shows ${}_rV_f$ for both M2 locations and at similar MNX operational parameters. The first feature seen from these measurements is an increasingly negative floating potential with increasing distance from the nozzle, until ring number 6 or 7. (Aperture plate M3 was typically several volts more positive than ring number 8.) The ${}_rV_f$ with the ER M2 is much lower than the MC M2. Recall that the HEP ions reach a much higher energy, $E_z \sim 70$ eV, with the ER M2 than the MC M2, $E_z \sim 30$ eV. Grounding M2 makes little difference in ${}_rV_f$. We attribute the large negative ${}_rV_f$ to an energetic electron population in the ER. When B_n was increased, the amplitude of ${}_rV_f$ fell by about a factor of 2 at full B_n field. An explanation for the effect on ${}_rV_f$ is that the fast electron population has a high pitch angle, *i.e.*, $v_\perp > v_{||}$. However, the most common explanation for hot electrons in helicon plasmas is Landau damping which generates high $v_{||}$[36].

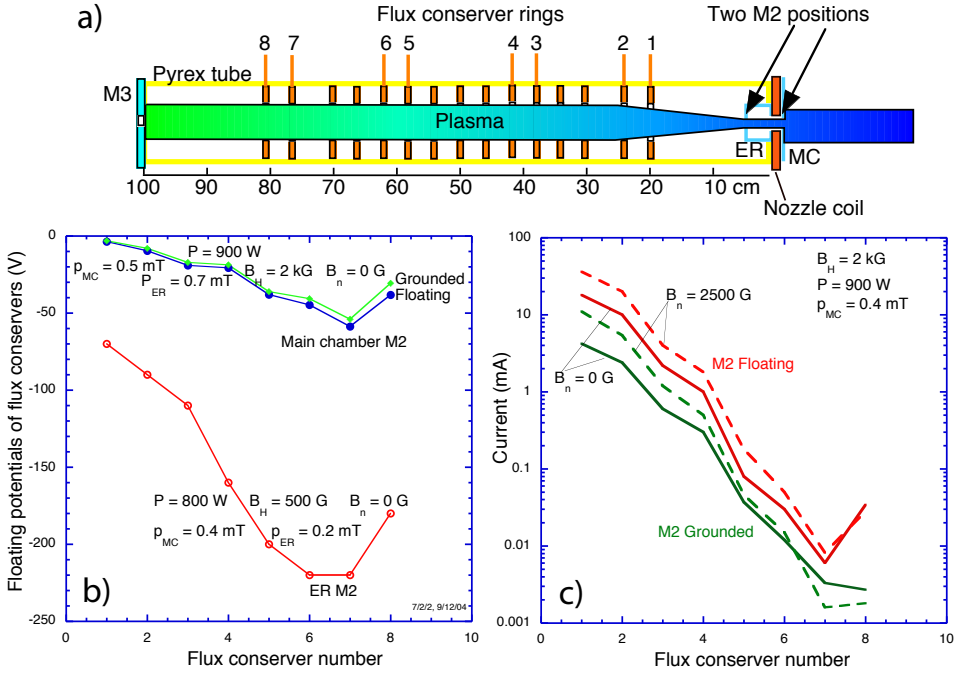

Figure 9: a) Schematic showing locations of 8 instrumented flux-conserver (copper) rings and the two positions of the M2 aperture plate used in this series of experiments. b) Floating potentials of 8 instrumented flux-conserver rings for two different M2 positions. The nozzle field was zero. Adding a nozzle field approximately halves the amplitude of the floating potentials. c) Current drawn by flux-conserver rings with and without the nozzle coil powered and with and without M2 grounded. The MC M2 position was used.

Fig. 9c) shows the effect on current to the rings with the rings biased at -1 volt. The expo-

nential decrease of current with distance is consistent with a linear decrease in floating potential, if the fast electron distribution is Maxwellian. The currents measured with a high nozzle field, though initially higher than with $B_n = 0$, decrease faster with distance, indicating a less energetic electron population in the ER with the nozzle field.

V. Spectroscopic measurements of electron energy

Using a 1/2-m J-A spectrometer equipped with an iCCD, spectra in the visible wavelength range were measured in the main chamber. Fig. 10a) shows the Abel-inverted brightness radial profiles of two lines, one for Ar I (763.5 nm) and the other for Ar II (434.8 nm). These measurements, made in the blue-core mode, show whence the blue core gets its name, from the strongly peaked bight blue of the argon ion lines. Fig. 10b) shows the ratio of brightnesses, $(B_{ArI})^2/B_{ArII}$, where B_i stand for the brightness of the i^{th} line. If collisional excitation were responsible for the emission, then $B_{ArI} = n_e n_{ArI} < \sigma v >_I$, $B_{ArII} = n_e n_{ArII} < \sigma v >_{II}$, and the ratio would be constant if the argon neutral density, n_{ArI}, and the electron-energy-distribution shape were independent of radius. The ratio is not constant, which could be explained by burnout of n_{ArI} on axis – estimated to be likely at the high densities in MNX – or if the relative population of the fast electrons changes with radius, for which we have no evidence. Burnout could explain the flattening of p_{ER} seen in Fig. 8a) with increasing B_n.

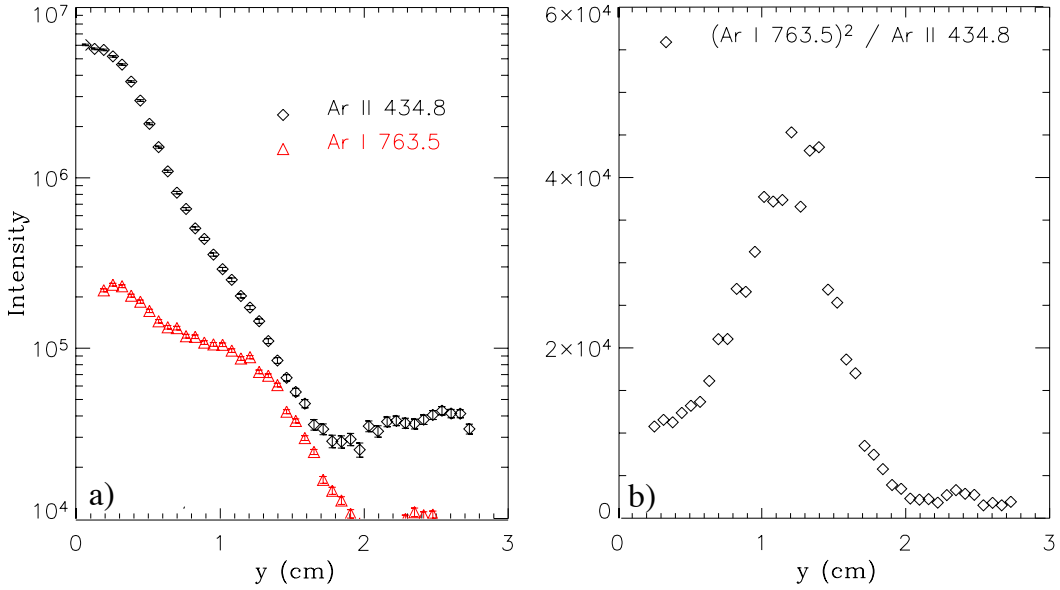

Figure 10: a) Abel-inverted brightnesses of an Ar I and an Ar II spectral line. b) Ratio of brightnesses, $(B_{ArI})^2/B_{ArII}$, as a function of radius.

If the plasma density is known, measurements of He I line ratios and use of a collisional-radiative model, such as that of Sasaki *et al.*[31], should allow the electron temperature to be calculated. A comparison of a "corrected" Sasaki model with experiment[37] showed very poor agreement at low density, $n_e < 10^{11}$ cm^{-3}, but improving agreement as the density approached 10^{12} cm^{-3}. At $T_e = 10$ eV and $n_e = 10^{12}$ cm^{-3}, the experimentally measured line ratios exceeded those expected based on the probe measurements by 20%[37], corresponding a temperature $\sim 10\%$ higher. We have confirmed the poor fit in the low density range but also found cases of good agreement for pure helium discharges at considerably higher density, $1-5\times10^{13}$ cm^{-3}, as predicted by the trend shown in Fig. 6 of Ref. [37]. Herein we present only select high-density cases which show great disagreements between probe measurements of T_e and line-ratio measurements. In our

experiments, probe measurements provided $n_e(r)$. As noted by [37], inclusion of a density profile improves the fit of the Sasaki model to the data.

The results of radial profile measurements are shown in Fig. 11a) in which we have used the original Sasaki model interpreted with our probe-measured central density. For Fig. 11a), the Sasaki method gives a twice higher electron temperature than the probes. Note that our use of the central density underestimates the temperature inferred from the line ratio model, hence the factor of 2 discrepancy is a lower limit. The discrepancy is even more pronounced under other operating conditions. Fig. 11b) compares the electron temperature using two lines ratios, 492.2 nm/471.3 nm and 504.8 nm/471.3 nm, with that obtained by the Langmuir probe. These discharges were prepared by starting with a pure helium helicon plasma, for which probes show a twice higher electron temperature than pure argon plasmas. To these plasma we added increasing flows of argon. The discharges were not in the blue-core mode. The Sasaki method is particularly susceptible to populations of fast electrons. The high temperatures indicated by the Sasaki method could be explained by a small population of 100-200 eV electrons added to a 5 eV Maxwellian. Collisions of He with Ar, not included in the Sasaki model, may also strongly affect the line ratios.

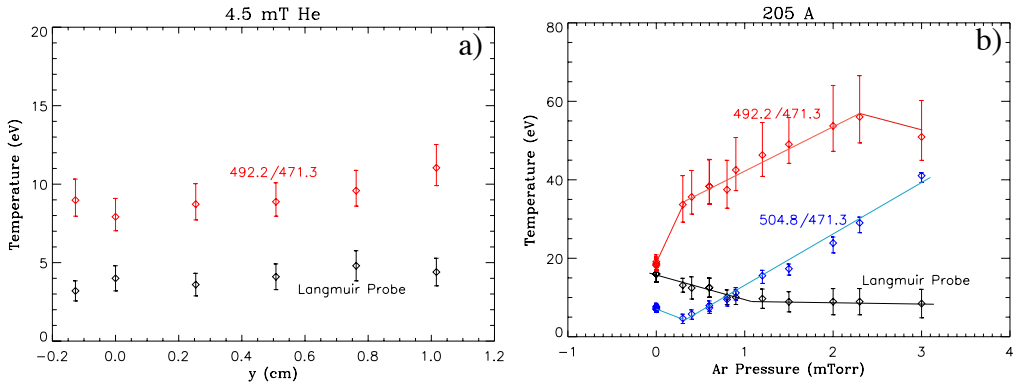

Figure 11: a) Radial profiles of T_e determined by the Sasaki *et al.* collisional-radiative model and with the Langmuir probe. b) The dependence of three calculated electron temperatures, using probe data and the Sasaki method, on argon fill pressure in a helium helicon discharge.

VI. Summary and future work

The LIF measurements show that a low temperature, high density – hence highly collisional – ion population exists in the MNX main chamber. A presheath accelerates these ions to above the sound speed, $E_z \sim T_e$, near apertures. This higher-than-expected energy is suggested to be the result of a superthermal electron population of energy $10T_e$ and density $0.003n_e$ in the main chamber[33]. Superthermal electron beams have been found in helicon plasmas by a number of research teams[38, 39, 40]. Whether the superthermal electrons are produced by Landau damping or by acceleration upstream through the double layer or by another mechanism is not resolved. The ions in the 2-4 cm long presheath retain their low parallel and perpendicular temperatures, *ca.* 0.1-1 eV, hence remain in equilibrium with each other. After passing through apertures, whether mechanical or magnetic, the ions are accelerated to superthermal speeds by a double layer of strength up to $\Delta\phi_{DL} \sim 3-10T_e$, also suggested to be the result of a tenuous superthermal electron population in the main chamber. The same attribution has been made for strong double layers found in lower density plasmas[22, 24]. As these superthermal ions flow through the expansion region (ER) they may interact with a cold ($T_i \sim 0.2$ eV), stagnant plasma formed by local ionization. Future research will examine whether such interactions lead to streaming instabilities.

Langmuir-probe characteristics in the ER (and main chamber) show a non-flat ion saturation current, extending beyond a bias voltage of -140 V. This may be attributable to a superthermal tail. The bulk electron temperature in the main chamber rarely exceeds 10 eV for Argon plasmas. Pure helium plasmas have a higher bulk temperature.

Floating potentials of macroscopic metal structures located in the main chamber and in the ER give convincing evidence for superthermal electrons. In particular, a series of copper rings in the ER reach floating potentials as great as -220 V. That the floating potentials become less negative with increasing nozzle field strength might occur if the fast electron population has a high pitch angle. The mechanism for creating a high pitch-angle distribution has not been found. The superthermal electrons are collisionless, as shown by the great distance in the ER at which the the large negative floating potentials occur. Probe measurements in the ER show a two-temperature electron distribution which is affected by the nozzle field.

One of the research goals of MNX is to explore the trajectories of ions as they are accelerated to speeds exceeding the Alfvén speed. The main question is whether the ions will stay on the field lines or detach. Theoretical work predicts detachment when the flow speed exceeds the Alfvén speed[14]. Fig. 12 shows the measured axial ion speed (black line) as a function of axial position for the same aperture arrangement as shown in Fig 5b). The nozzle coil is located at z = 0 cm. Measurements of ion speed stopped about 10 cm from the nozzle due to low LIF signal strength. At the furthest point from the nozzle where there was good LIF signal-to-noise, the ion energy was about 75 eV. In these experiments the floating potential of the copper rings reached -200 volts. Based on this we extrapolate the ion velocity for both Ar^{+} and Ar^{+2} (dashed black lines).

Also shown in Fig. 12 are the axial field strength and the local Alfvén speed, calculated under the assumption that the plasma density decreases with distance proportional to B/v, where v is the ion flow speed and B the magnetic field strength. The large jump in the Alfvén speed immediately downstream of the nozzle is due to the steep drop in plasma density at the double layer. Fig. 12 shows that the ion speed is expected to reach the Alfvén speed about 40 cm from the nozzle coil for Ar^{+} and 30 cm for Ar^{+2}. Studies of super-Alvénic ion flows in MNX will require reduction in background gas pressure and increases in LIF detection efficiency, to compensate for the diminished signal at increasing distance from the nozzle. Other technical challenges will have to be addressed to perform these important experiments.

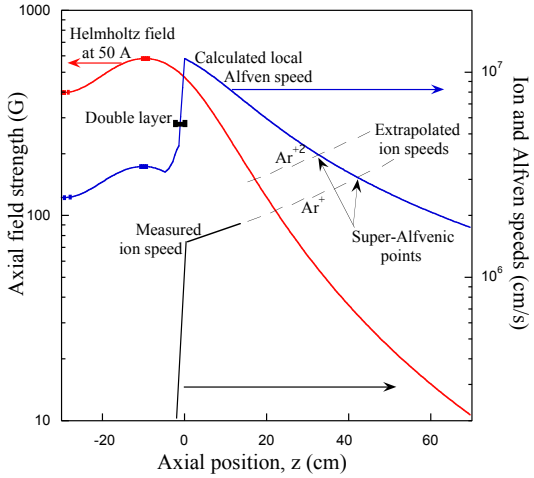

Figure 12: Axial field strength (red), measured flow speed (black solid line), calculated Alfvén speed (blue) and extrapolated flow speeds (dashed black lines) for both Ar^{+} and Ar^{+2} are shown.

Acknowledgements: This work was supported, in part, by the U.S. Department of Energy Contract No. DE-AC02-76-CHO-3073. The WVU portion of this work was supported by the U.S. Department of Energy EPSCoR Laboratory Partnership Program under Grant No. ER45849. We thank Bruce Berlinger for excellent technical support and Dr. Y. Raitses for useful conversations.

a) Princeton Plasma Physics Laboratory, Princeton University
b) Physics Department, West Virginia University
c) University Research Program in Robotics, University of Michigan
d) Air Force Research Laboratory, Wright-Patterson Air Force Base
e) Physics Department, Auburn University

References

[1] Francis F. Chen and Rod W. Boswell. "Helicons – The Past Decade". *IEEE Transactions on Plasma Science*, 25:1245, 1989.

[2] Rod W. Boswell and Francis F. Chen. "Helicons – The Early Years". *IEEE Transactions on Plasma Science*, 25:1229, 1989.

[3] M. A. Lieberman and A. J. Lichtenberg. *Principles of Plasma Discharges and Materials Processing*. John Wiley and Sons, Inc., New York, 1994.

[4] A.J. Perry, D. Vender, and R.W. Boswell. "The application of the helicon source to plasma processing". *J. Vac. Sci. and Technol. B*, 9:310, 1991.

[5] B. P. Cluggish, F. A. Anderegg, R. L. Freeman, J. Gilleland, T. J. Hilsabeck, R. C. Isler, W. D. Lee, A. A. Litvak, R. L. Miller, T. Ohkawa, S. Putvinski, K. R. Umstadter, and D. L. Winslow. "Density profile control in a large diameter helicon plasma". *Physics of Plasmas*, 12:57101, 2005.

[6] A. Komori, T. Shoji, M. Miyamoto, J. Kawai, and Y. Kawai. "Helicon waves and efficient plasma production". *Physics of Fluids B*, 3:893, 1991.

[7] F. F. Chen. "Plasma ionization by helicon waves". *Plasma Physics and Controlled Fusion*, 33:339, 1991.

[8] F. Chang-Diaz. "The VASIMR rocket". *Scientific American*, 283:90, 2000.

[9] James A. Gilleland. "Application of a Helicon Discharge to Electric Propulsion". *AIAA*, 98:3934, 1998.

[10] Robert H. Frisbee. "Advanced Plasma Propulsion for the 21st Century". *Journal of Propulsion and Power*, 19:1129, 2003.

[11] Robert G. Jahn and Edgar Y. Choueiri. "Electric Propulsion"*, in Encyclopedia of Physical Science and Technology, Third Edition*. Academic Press, New York, 2002.

[12] E.B. Hooper. "Plasma detachment from a magnetic nozzle". *Journal of Propulsion and Power*, 9:757, 1993.

[13] S. A. Cohen, N. S. Siefert, S. Strange, R. F. Boivin, E. E. Scime, and F. M. Levinton. "Ion acceleration in plasmas emerging from a helicon-heated magnetic-mirror device". *Physics of Plasmas*, 10:2593, 2003.

[14] A. V. Arefiev and B. N. Breizman. "Theoretical components of the VASIMR plasma propulsion concept". *Physics of Plasmas*, 11:2942, 2004.

[15] M.D. Carter, F.W. Baity Jr., G.C. Barber, R.H. Goulding, D.O. Spareks, K.F. White, and E.F. Jaeger. "Comparing experiments with modeling for light ion helicon plasma sources". *Physics of Plasmas*, 9:5097, 2002.

[16] Andrew Ilin, Frankin Chang Diaz, Jared Squire, and Mark D. Carter. "Plasma Heating Simulation in the VASIMR System". *AIAA*, 2005.

[17] C. Charles and R. W. Boswell. "Current-free double-layer formation in a high-density helicon discharge". *Applied Physics Letters*, 82:1356, 2003.

[18] L. R. Block. "A double layer review". *Astrophysics and Space Science*, 55:59, 1978.

[19] N. Hershkowitz. "Review of recent laboratory double layer experiments". *Space Science Reviews*, 41:351, 1985.

[20] M. A. Raadu. "The physics of double layers and their role in astrophysics". *Physics Reports*, 178:25, 1989.

[21] G. Hairapetian and R. Stenzel. "Observation of a stationary, current-free double layer in a plasma". *Physical Review Letters*, 65:175, 1990.

[22] G. Hairapetian and R. Stenzel. "Particle dynamics and current-free double layers in an expanding, collisionless, two-electron-population plasma". *Physics of Fluids B*, 3:899, 1991.

[23] R. Schrittwieser, I. Axnas, T. Carpenter, and S. Torven. "Observation of double layers in a convergent magnetic field". *IEEE Trans. on Plasma Science*, 20:607, 1992.

[24] K. Sato and F. Miyawaki. "Formation of presheath and current-free double layer in a two-electron-temperature plasma". *Physics of Fluids***B**, 4:1247, 1992.

[25] N. Plihon, C. S. Corr, and P. Chabert. "Double layer formation in the expanding region of an inductively coupled electronegative plasma". *Applied Physics Letters*, 86:091501, 2005.

[26] X. Sun, A. M. Keesee, C. Biloiu, E. E. Scime, A. Meige, C. Charles, and R. W. BOswell. "Observations of Ion-Beam Formation in a Current-Free Double Layer" . *Physical Review Letters*, 95:025004, 2005.

[27] Xuan Sun, Earl Scime, Mahmood Miah, Samuel Cohen, and Frederick Skiff. "Measurement of Asymmetric Optical Pumping of Ions Accelerating in a Magnetic Field Gradient". *Physical Review Letters*, 93:23502, 2004.

[28] G.D. Severn, D.A. Erlich, and R. McWilliams. "Argon ion laser-induced fluorescence with diode lasers". *Rev. Sci. Instrum.*, 69:10, 1998.

[29] R. F. Boivin and E. E. Scime. "Laser induced fluorescence in Ar and He plasmas with a tunable diode laser". *Rev. of Sci. Instrum.*, 74:4352, 2003.

[30] R.L. Kurucz and B.Bell. "1995 Atomic Line data". *Smithsonian Astrophysical Observatory, CD-ROM No.23*, 1995.

[31] Satoshi Sasaki, Shuichi Takamura, Shinichi Watanabe, Suguru Masuzaki, Takako Kato, and Kiyoshi Kadota. "Helium I line intensity ratios in a plasma for the diagnostics of fusion edge plasmas". *Rev. Sci. Instrum.*, 67:3521, 1996.

[32] R. F. Boivin. 'Zeeman Splitting for LIF Transitions and De-convolution Technique to Extract Ion Temperature'". *EPAPS Deposited Document*, E-PHPAEN-10-003306, 2003.

[33] Xuan Sun, S.A. Cohen, Mahmood Miah, and Earl Scime. "On-axis parallel ion speeds near mechanical and magnetic apertures in a helicon plasma devices". *in preparation*, 2005.

[34] K. Shiraishi and S. Takamura. "Sheath formation in the SOL plasma with energetic electrons". *Journal of Nuclear Materials*, 176 and 177:251, 1990.

[35] M. Cercek and T. Gyergyek. "Collector floating potentials in a discharge plasma". *Journal of Physics D*, 34:330, 2001.

[36] F. F. Chen and D. D. Blackwell. "Upper limit to Landau damping in helicon discharges". *Physical Review Letters*, 82:2677, 1999.

[37] R. F. Boivin, J. L. Kline, and E. E. Scime. "Electron temperature measurement by a helium line intensity ratio method in helicon plasmas". *Phys. Plasmas*, 8:5303, 2001.

[38] Shane M. Tysk, C. Mark Denning, John E. Scharer, and Kamran Akhtar. "Optical, wave measurements, and modeling of helicon plasmas for a wide range of magnetic fields". *Physics of Plasmas*, 11:878, 2004.

[39] Robert Tseng Shiung Chen and Noah Hershkowitz. "Multiple Electron Beams Generated by a Helicon Plasma Discharge". *Phys. Rev. Lett.*, 80:4677, 1998.

[40] Peiyuan Zhu and R. W. Boswell. "Observation of nonthermal electron tails in an rf excited argon magnetoplasma". *Phys. Fluids B*, 3:869, 1991.